CHIN. PHYS. LETT. Vol. 38, No. 1 (2021) 015201

Nitrogen and Boron Co-Doped Carbon Nanotubes Embedded with Nickel Nanoparticles as Highly Efficient Electromagnetic Wave Absorbing Materials

Xin Zhu(朱鑫)[1], Feng Yan(闫峰)[1*], Chunyan Li(李春燕)[1], Lihong Qi(齐立红)[1], Haoran Yuan(袁浩然)[1], Yanfeng Liu(刘岩峰)[2], Chunling Zhu(朱春玲)[2*], and Yujin Chen(陈玉金)[1,2,3*]

[1]*Key Laboratory of In-Fiber Integrated Optics (Ministry of Education), and College of Science, Harbin Engineering University, Harbin 150001, China*
[2]*College of Materials Science and Chemical Engineering, Harbin Engineering University, Harbin 150001, China*
[3]*School of Materials Science and Engineering, Zhengzhou University, Zhengzhou 450001, China*

(Received 20 September 2020; accepted 9 November 2020; published online 6 January 2021)

Due to the limitations of impedance matching and attenuation matching, carbon nanotubes (CNTs) employed alone have a weak capacity to attenuate electromagnetic wave (EMW) energy. In this work, B and N co-doped CNTs with embedded Ni nanoparticles (Ni@BNCNTs) are fabricated via an *in situ* doping method. Compared with a sample without B doping, Ni@BNCNTs demonstrate a superior EMW absorption performance, with all minimum reflection loss values below −20 dB, even at a matching thickness of 1.5 mm. The experimental and theoretical calculation results demonstrate that B doping increases conduction and polarization relaxation losses, as well as the impedance matching characteristic, which is responsible for the enhanced EMW absorption performance of Ni@BNCNTs.

DOI: 10.1088/0256-307X/38/1/015201

The development of high-performance electromagnetic wave absorbing materials has become increasingly important, due to the seriously increase in electromagnetic pollution. Carbon materials, including carbon fiber,[1] graphene,[2] carbon nanotubes (CNTs),[3] and carbon-ferrite composites have been fabricated as lightweight electromagnetic wave absorbers, by virtue of their relatively low mass density. Of these carbon materials, CNTs have attracted widespread attention, due to their hollow structure.[4,5] However, it is difficult to achieve an improved impedance matching characteristic in CNTs due to a lack of magnetic loss. Therefore, many methods have been developed to couple CNTs with magnetic metals in order to improve the overall impedance matching performance.[6–11] For example, Lin *et al.* prepared a composite composed of CNTs and Fe particles, finding that the composite exhibited superior electromagnetic wave absorption properties in comparison to pristine CNTs.[7] Qing *et al.* used CNTs and carbonyl iron as precursors to produce an epoxy silicone resin/CNT/carbonyl iron composite which exhibited highly effective electromagnetic shielding properties.[8] Li *et al.* coated Fe_3O_4 magnetic nanoparticles onto CNTs, discovering that the CNT/Fe_3O_4 had a minimal reflection loss of −28.7 dB.[9] Shen *et al.* fabricated a CNT/Ni composite with a minimal reflection loss of −22.89 dB at 11.4 GHz.[10] However, the magnetic materials on the CNT surfaces were prone to agglomeration and tended to suffer from oxidation and/or acidic/alkaline corrosion, limiting their practical applications. Magnetic metal nanoparticles embedded in N-doped CNTs (M@NCNTs) could address the issues mentioned above.[12–16] Li *et al.* prepared three-dimensional (3D) M@NCNTs via a simple method. Their results demonstrated a minimum reflection loss in the composites of 49.82 dB at a frequency of 7.92 GHz, where the effective absorption bandwidth was 4 GHz.[14] Zhang *et al.* fabricated a CoNi-nanoparticle-encapsulated NCNT array on an rGO sheet by means of a simple vacuum freeze-drying process and a subsequent carbonization process. The resulting unique 3D structure exhibited excellent electromagnetic wave absorption properties due to its large surface, abundant defects, various interfaces and void spaces, and nitrogen dopants.[16] Nevertheless, the electrical conductivities of the absorbers mentioned above were too high, and thereby the impedance matching characteristics needed to be precisely controlled.

Recently, N,B co-doped carbon-based materials have demonstrated significantly enhanced catalytic activity due to a tuned electronic structure of adjacent carbon atoms by means of dual-atom dopants.[17,18] Charge redistribution arising due to changes in the

Supported by the National Natural Science Foundation of China (Grant No. 51972077), the Heilongjiang Touyan Innovation Team Program, and the Fundamental Research Funds for the Central Universities (Grant Nos. 3072020CF2518, 3072020CFT2505, and 3072020CFJ2503).
*Corresponding author. Email: chenyujin@hrbeu.edu.cn; yanfeng@hrbeu.edu.cn; zhuchunling@hrbeu.edu.cn
© 2021 Chinese Physical Society and IOP Publishing Ltd

electronic structure can induce dipole polarizations, and thus may good candidates for improving the electromagnetic wave absorption properties of magnetic/carbon nanotubes. Furthermore, the increased number of defects formed due to N,B co-doping could serve as polarization centers, which may facilitate an increase in dielectric loss, thereby improving the electromagnetic wave absorption capability of the magnetic/carbon nanotubes.[19] However, N,B co-doped carbon materials containing embedded magnetic metals have rarely been reported for electromagnetic wave absorption.

In this Letter, we fabricate N,B co-doped NCNTs with embedded Ni nanoparticles (Ni@BNCNTs) as advanced electromagnetic wave absorbers, using a simple method. The as-fabricated Ni@BNCNTs offer the following advantages in terms of electromagnetic wave absorption: (i) There are abundant interfaces between Ni nanoparticles and BNCTs in the Ni@BNCNTs, facilitating improvements in relation to interfacial polarizations;[20] (ii) a larger number of defects are introduced into the Ni@BNCNTs due to B,N co-doping, facilitating the improvement of dipole polarizations;[21] (iii) B,N co-doping can improve the impedance matching characteristic, thereby favoring the propagation of increased electromagnetic waves in absorbers based on Ni@BNCNTs; (iv) the metallic Ni nanoparticles are encapsulated within BNCNTs, conferring a robust stability on the metal nanoparticles in terms of oxidation. As a result, the optimized Ni@BNCNT exhibits superior electromagnetic wave absorption properties with a minimal reflection loss of -37.5 dB at a matching thickness of 2.5 mm, and an efficient absorption bandwidth of 3.92 GHz at a matching thickness of 1.5 mm.

The detailed synthesis processes, structural characteristics of the samples, and electromagnetic parameters utilized in this work can be found in the Supplementary Information. Figure 1 illustrates the synthesis process of our Ni@BNCNTs. The precursors for the Ni@BNCNTs were obtained by stirring a solution containing $NiCl_2{\cdot}6H_2O$ and $NaBH_4$ in a protective Ar atmosphere. The precursors were then mixed with dicyandiamide (DCD) with a mass ratio of 1 : 30, and the mixture was heated to different temperatures under an Ar flow. During the synthesis process, the DCD furnished the C and N sources, and the Ni species served as catalysts for the growth of the NCNTs. Due to the presence of B species, the B atoms were doped into the CNTs *in situ*. In this way, we were successfully able to fabricate our Ni@BNCNTs. For convenience, samples fabricated at 700, 800, and 900℃ were designated as Ni@BNCNT-700, Ni@BNCNT-800 and Ni@BNCNT-900, respectively. For comparison, Ni@NCNT-800 without B dopants was also fabricated, using $Ni(OH)_2$ as precursor at 800℃ under similar conditions.

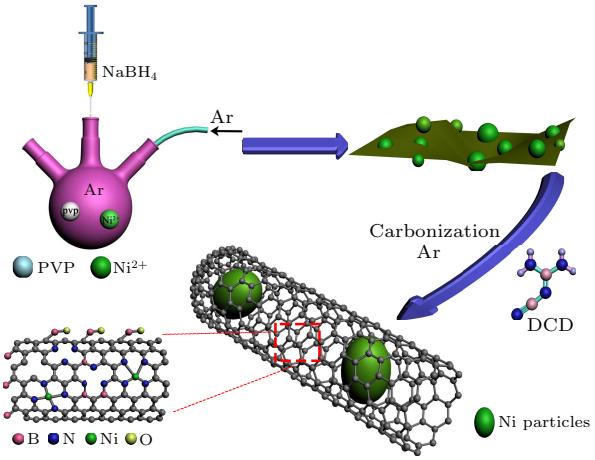

Fig. 1. Schematic illustration of the formation process of Ni@BNCNTs.

The results of x-ray diffraction (XRD) show that the precursors for the Ni@BNCNTs contain Ni_2B and $Ni(OH)_2$ (JCPDS No. 48–1222 and JCPDS No. 73–1520), while the precursors for Ni@NCNT-800 are composed of $Ni(OH)_2$ (JCPDS No. 73–1520) alone (see Fig. S1 in the Supplementary Material). Scanning electron microscopy (SEM) images indicate that the precursors for the Ni@BNCNTs comprise a mixture of nanosheets and nanoparticles, corresponding to Ni_2B and $Ni(OH)_2$, respectively (Fig. S2a). The SEM images reveal that the $Ni(OH)_2$ precursors exhibit a severely aggregated particle-like morphology (Fig. S2b). Following high-temperature treatment with the assistance of the DCD, these precursors were transformed into Ni-nanoparticle-encapsulated NCNTs. Figure 2(a) shows the XRD patterns of Ni@BNCNTs and Ni@NCNT-800. The diffraction peaks of the as-prepared samples at 44.5°, 51.8°, and 76.4° correspond to the (111), (200), and (220) planes of metallic Ni (JCPD card No. 04–0850), respectively. The crystallite size of the metal particles can be calculated according to the Scherrer formula: $D = 0.9\lambda/\beta\cos\theta$. Analyzing the XRD spectrum information using Jade software, the parameter values for the above formula can then be obtained, leading to a calculated crystallite size, D, of 17.2 nm. In addition, a strong carbon diffraction peak at about 26.1° can be observed in the XRD patterns, which corresponds to the (002) crystal plane of graphitic carbon. Negligible differences in the diffraction peak positions indicate that Ni@BNCNTs and Ni@NCNT share similar crystalline compositions. Figure 2(b) shows the Raman spectra of the as-prepared Ni@BNCNTs and Ni@NCNT-800. Two peaks, centered at 1360 cm^{-1} and 1590 cm^{-1}, correspond to the G band (the stretching vibration of the C atom's sp^3 hybridization) and the D band (the stretching vibration of the C atom's

sp^2 hybridization in the plane), respectively. The intensity ratios from the D band to the G band (I_D/I_G) for Ni@BNCNT-700, Ni@BNCNT-800, and Ni@BNCNT-900 are 0.932, 0.914, and 0.899, respectively, lower than that of Ni@NCNT-800 (0.938). This indicates that Ni@BNCNTs possess more defects, which may be due to B doping.

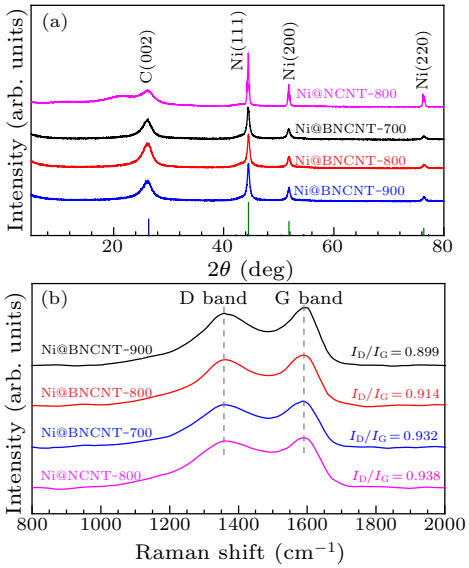

Fig. 2. (a) XRD patterns and (b) Raman spectra of Ni@NCNT-800 and Ni@BNCNTs.

SEM images reveal that the lengths and diameters of NCNTs in both Ni@BNCNT-800 and Ni@NCNT-800 measure several micrometers and about 60 nm, respectively [Figs. 3(a) and 3(c) and Figs. S3a and S3d]. However, the NCNTs in Ni@BNCNT-800 display a more uniform morphology and size, which may be attributed to the enhanced dispersity of its precursors, together with the presence of B species, which may have affected the growth rate of the NCNTs.[22] Transmission electron microscopy (TEM) images indicate that the NCNTs in Ni@BNCNT-800 and Ni@NCNT-800 exhibit bamboo-like morphologies, with the Ni NPs encapsulated within the channels of the NCNTs [Fig. 3(b) and Fig. S3d]. The Ni NPs have an average diameter of 30 nm in Ni@BNCNT-800 and Ni@NCNT-800 [Fig. 3(b) and Fig. S3d]. Notably, the magnetic NPs are isolated because they are confined within the channels of the NCNTs, which is conducive to the suppression of the eddy current loss at high frequency bands.[23,24] The wall thicknesses of the NCNTs and the periodic distance of the adjacent "bamboo" are about 6 nm and 60 nm, respectively [Figs. 3(c) and 3(d) and Figs. S3d and S3e]. Thus, there are lots of closed nanosized void spaces, facilitating an improvement in electromagnetic wave absorption properties.[16,25] The high resolution TEM (HRTEM) images depict interplanar spacings relating to the Ni NPs and the nanotube walls of the NCNTs for Ni@BNCNT-800 and Ni@NCNT-800 of 0.204 and 0.338 nm, corresponding to the (111) plane of metallic Ni and the (002) plane of graphitic carbon, respectively [see Figs. 3(e) and 3(f), and Fig. S3f]. Defects can clearly be observed in the nanotube walls, indicated by blue circles in Figs. 3(e) and 3(f) and Fig. S3f. These defects may induce polarization relaxation, which is conducive to the electromagnetic wave absorption of both Ni@BNCNT and Ni@NCNT-800. In addition, the NCNTs in Ni@BNCNT-700 have similar sizes to those of the NCNTs in Ni@BNCNT-800 (see Fig. S3b). However, some larger NCNTs are observed in the SEM image of Ni@BNCNT-900 (see Fig. S3c). The Ni content of Ni@BNCNT-700, Ni@BNCNT-800, Ni@BNCNT-900, and Ni@NCNT-800 measures 8.21 wt%, 6.18 wt%, 5.86 wt%, and 6.75 wt%, respectively. The decreased Ni content in the Ni@BNCNT fabricated at a higher carbonization temperature is attributed to the favorable growth of NCNTs at higher temperatures.[15,16,23]

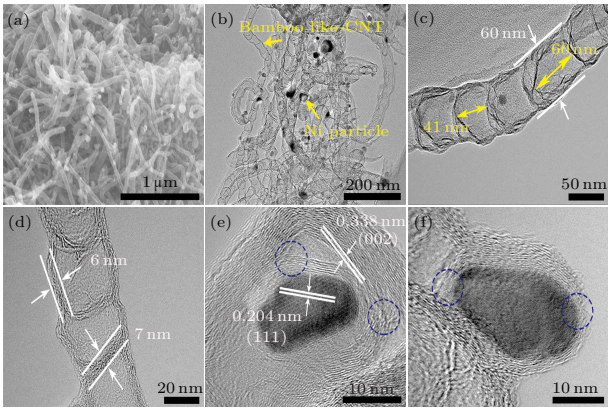

Fig. 3. (a) SEM image, (b)–(d) TEM images, (e) and (f) HRTEM images of Ni@BNCNT-800.

X-ray photoelectron spectroscopy (XPS) was performed to obtain surface information for Ni@BNCNT-800 and Ni@NCNT-800. A B signal can be observed in the survey spectra of Ni@BNCNT-800, but not in Ni@NCNT-800, suggesting the successful introduction of B into Ni@BNCNT-800 (Fig. S4). Figure S5a shows the Ni 2p XPS spectra of Ni@BNCNT-800 and Ni@NCNT-800. The peaks at 853.0 and 870.0 eV correspond to metallic Ni, while the peaks at 854.9 and 872.6 eV, as well as satellite peaks at 861.45 and 880.13 eV, can be assigned to Ni, specifically the Ni^{2+} $2p_{3/2}$ and Ni^{2+} $2p_{1/2}$ orbits, respectively.[26] The signals of oxidation state Ni species are attributed to the oxidation of samples on exposure to air, or the existence of Ni-N_x species. Also present in the N 1s spectra of Ni@BNCNT-800 and Ni@NCNT-800 are pyridine-N (398.7 eV), Ni–N_x bonds (399.3 eV), pyrrole-N (400.2 eV), quaternary nitrogen (401.3 eV), nitrogen oxide (403.0 eV), and chemisorbed nitrogen (406.3 eV) (see Fig. S5b).[15,27] In addition, one addi-

tional peak at 397.6 eV appears in the N 1*s* spectra of Ni@BNCNT-800, which can be ascribed to the N–B species.[28] In addition, the B 1*s* XPS spectrum of Ni@BNCNT-800 displays three peaks. The first peak corresponds to B–C, while the other two, at 190.5 and 192.3 eV respectively, are assigned to O–B–C bonds (Fig. S5c).[29] Thus, both the B 1*s* and N 1*s* spectra demonstrate that both N and B are doped into the CNTs in Ni@BNCNT-800. The N and B contents in Ni@BNCNT-800 are estimated to be 9% and 2% in terms of the XPS data, respectively, while the N content in Ni@NCNT-800 is about 11%. The magnetic properties of the Ni@BNCNTs and Ni@NCNT-800 were measured using a sample vibration magnetometer at room temperature. The hysteresis loops of the Ni@BNCNT-800 and Ni@NCNT-800 indicate their weak ferromagnetic character (Fig. S6). The saturation magnetization (M_s) of Ni@BNCNT-800 is 5.91 emu/g, lower than that of Ni@NCNT-800 (M_s = 13.31 emu/g), relevant to their corresponding Ni contents. In contrast, the coercive force (H_c) of Ni@BNCNT-800 is 72.52 Oe, larger than that of Ni@NCNT-800 (H_c = 51.94 Oe), due to B doping.

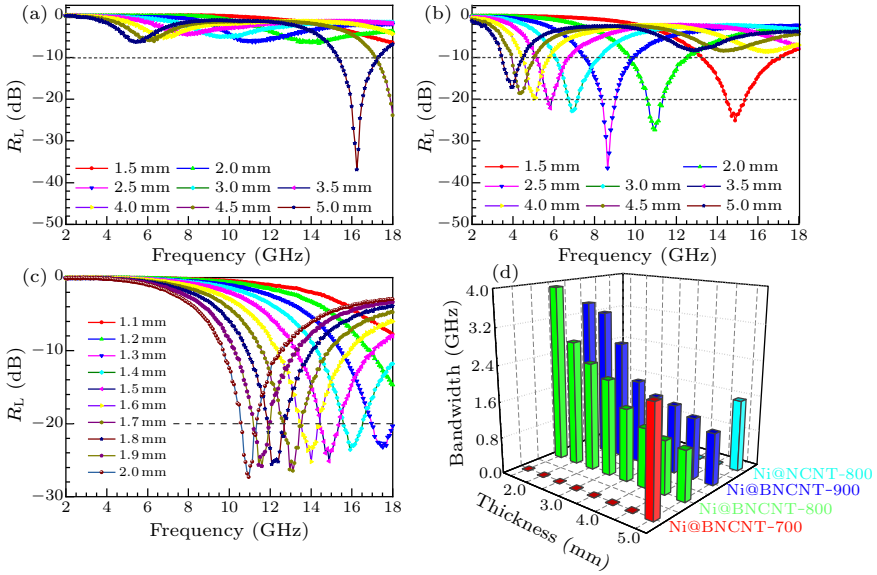

Fig. 4. Frequency-dependent R_L of (a) Ni@NCNT-800 and (b) Ni@BNCNT-800 at d in the range 1.5–5.0 mm. (c) Calculated frequency-dependent R_L of Ni@BNCNT-800 at d in the range 1.1–2.0 mm, and (d) absorption bandwidth for various sample thicknesses.

The reflection loss (R_L) of each sample was calculated based on the electromagnetic parameters measured by a vector network analyzer:[30]

$$Z_{in} = Z_0\sqrt{\frac{\mu_r}{\varepsilon_r}}\tanh\left(\frac{j2\pi fd}{c}\times\sqrt{\mu_r\varepsilon_r}\right), \quad (1)$$

$$R_L = 20\log\left|\frac{Z_{in}-Z_0}{Z_{in}+Z_0}\right|, \quad (2)$$

where Z_{in} and Z_0 denote the input impedance of the absorber and the impedance of free space, respectively; $\varepsilon_r = \varepsilon' - j\varepsilon''$ represents the relative complex permittivity; $\mu_r = \mu' - j\mu''$ is the relative complex permeability; c is the speed of the electromagnetic wave in free space; f is the frequency of the electromagnetic wave; and d is the matching thickness of the absorber. Notably, when the R_L values reach −10 and −20 dB, 90% and 99% of the electromagnetic wave energy are consumed by the absorber, respectively. Therefore, for improved electromagnetic wave absorption, the minimum value of R_L must be less than −10 dB. In order to compare intuitively, we adjusted all additional amounts of absorbents, which were controlled to 25 wt%.

According to the quarter-wavelength elimination model, the thickness of the absorber satisfies the formula $d = n\lambda/4 = nc/(4f\sqrt{|\mu_r\varepsilon_r|})$, $n = 1, 3, 5\ldots$, where λ represents the wavelength of electromagnetic waves. At this time, the absorber experiences a maximum reflection loss R_L at a certain frequency. According to the above formula, it can be concluded that as the thickness of the absorber increases, the matching frequency moves to the low frequency region. It is precisely due to the contribution of the quarter-wavelength interference characteristics that the matching thickness and absorption peak frequencies conform to the electromagnetic wave absorption characteristics. Figures 4(a) and 4(b) show the variation of R_L for Ni@NCNT-800 and Ni@BNCNT-800 with an increase in frequency over a range 2–18 GHz. It transpires that the R_L values of Ni@NCNT-800 exceed −10 dB only when the matching thickness is greater than 4.5 mm, revealing an inferior electromag-

netic wave absorption capability. In contrast, the minimal R_L values of Ni@BNCNT-800 can reach −10 dB at a matching thickness of 1.5–2.0 mm, and exceed −20 dB when the thickness is in a range 1.5–4.0 mm; when d is 2.5 mm, the R_L value reaches −37.5 dB, and the absorber can attenuate nearly 99.99% of the electromagnetic wave energy, which confirms the ideal wave absorption performance of this material. Based on the figure, we can also observe that the minimum R_L values of Ni@BNCNT-800 and Ni@BNCNT-900 are in the low frequency range (2–9 GHz), which meets the standard of effective low-frequency absorption required for today's absorbing materials. Moreover, both Ni@BNCNT-700 and Ni@BNCNT-900 also exhibit enhanced electromagnetic wave absorption capabilities with respect to Ni@NCNT-800, suggesting that B doping is an efficient method of improving the material's electromagnetic wave absorption capability (Fig. S7). Furthermore, even when the matching thickness is in a range of 1.1–2.0 mm, the minimal R_L values of Ni@BNCNT-800 reach −20 dB, and the effective absorption bandwidth (EAB_{10}) is up to 3.92 GHz at $d = 1.5$ mm [Figs. 4(c) and 4(d)], which are favorably comparable or superior results to those achieved for most reported magnetic metal/carbon composites (see Table S1).[31] Therefore, Ni@BNCNT-800 represents a satisfactory candidate to act as a lightweight EMW absorber.

For a conductive absorber, its ε'' generally includes conduction (ε''_c) and polarization relaxation loss (ε''_p). To elucidate the origin of Ni@BNCNT-800's enhanced dielectric loss performance, we simulated ε' and ε'' based on a modified Havriliak–Negami (H-N) model:[32]

$$\varepsilon = \varepsilon_\infty + \frac{\varepsilon_s - \varepsilon_\infty}{[1 + (j\omega\tau)^{1-\alpha}]^\beta} - j\frac{\sigma}{\varepsilon_0\omega^t}, \quad (0 \leqslant \alpha < 1,\ 0 < \beta \leqslant 1,\ 0 < t \leqslant 1) \tag{3}$$

where ε_0 is the permittivity of free space, ε_∞ and ε_s denote the relative permittivity at the high frequency limit and static permittivity, respectively, τ represents polarization relaxation time, σ represents conductivity, ω represents the angular frequency, t stands for an index indicating ohmic behavior, β represents the asymmetry factor related to the relaxation of the interface, and α is a constant relative to the number of relaxation processes. If α is equal to 0, a single relaxation process will occur in an absorber in response to electromagnetic wave radiation, while $\alpha > 0$ indicates that multiple dielectric relaxation processes occur.

To explain the enhanced electromagnetic wave absorption properties of the Ni@BNCNTs, we compare the respective ε_r and μ_r values of Ni@BNCNT-800 and Ni@NCNT-800. As shown in Figs. 5(a) and 5(b), Ni@BNCNT-800 has larger ε' and ε'' values than Ni@NCNT-800. Furthermore, the dielectric loss tangent ($\tan\delta_e = \varepsilon''/\varepsilon'$) values of Ni@BNCNT-800 are in a range of 0.26–0.46, far greater than those of Ni@NCNT-800 (0.13–0.18) [Fig. 5(c)]. Thus, the Ni@BNCNT-800 exhibits an enhanced dielectric loss performance, which improves its electromagnetic wave absorption capability.[33,34] By simulating the calculated values using Eq. (3), it is evident that the calculated values are in good agreement with those measured experimentally. The crucial simulated parameters are listed in Table S2. The α and β of Ni@BNCNT-800 and Ni@NCNT-800 are larger than 0, indicating that multiple relaxations containing interfacial polarization contribute to their dielectric losses,[35] as confirmed by the Cole–Cole plots [Fig. 5(d)].

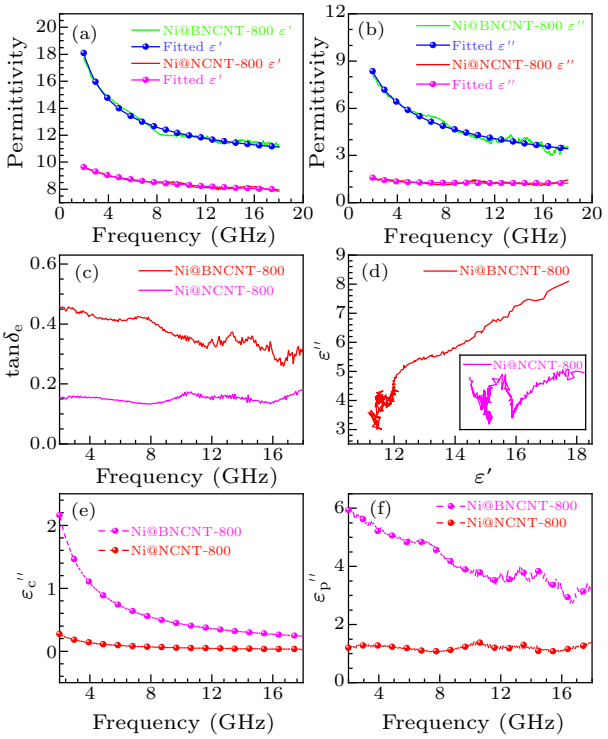

Fig. 5. (a) Experimental measured and fitted real parts, and (b) experimental measured and fitted imaginary parts of the complex permittivities for Ni@BNCNT-800 and Ni@NCNT-800; (c) dielectric loss tangents and (d) Cole–Cole plots for Ni@BNCNT-800 and Ni@NCNT-800; (e) ε''_c–f and (f) ε''_p–f plots for Ni@BNCNT-800 and Ni@NCNT-800.

In addition, the defects and the functional groups at the NCNT surfaces can serve as polarization centers, so that dipole polarization partially contributes to the dielectric loss in Ni@BNCNT-800 and Ni@NCNT-800. The t value of Ni@BNCNT-800 is 0.49, larger than that of Ni@NCNT-800 (0.10), indicating the formation of a superior conductive network in Ni@BNCNT-800 to that present in Ni@NCNT-800. This is also confirmed by the higher electrical conductivity in Ni@BNCNT-800 (0.24 S/m) in contrast

to that of Ni@NCNT-800 (0.03 S/m). Thus, the ε_c'' ($\varepsilon_c'' = \sigma/\varepsilon_0\omega^t$) values of Ni@BNCNT-800 are higher than those of Ni@NCNT-800 [Fig. 5(e)], particularly in the low frequency region. Based on the ε_c'' and ε'' data, the ε_p'' values of samples can be extracted. As shown in Fig. 5(f), Ni@BNCNT-800 has larger ε_p'' values than Ni@NCNT-800 over a frequency range 2–18 GHz. Therefore, the introduction of B improves both conduction and polarization relaxation losses underlying the enhanced electromagnetic wave absorption properties of Ni@BNCNT-800.

To shed light on this interfacial polarization, we calculated the charge distribution of Ni and C atoms at the interface between Ni NPs and BNCNTs (for detailed calculated data, see the Supplemental Materials). Figures 6(a) and 6(b) contain the structural models of B,N-doped graphene and Ni clusters close to NCNTs, respectively. The calculation results are shown in Figs. 6(c) and 6(d), where the regions indicated by the blue and yellow colors denote hole-rich and electron-rich domains, respectively. According to the isosurface diagram of the change in charge density, we can see that obvious charge redistribution occurs at the interfaces between metal Ni and BNCNT. The charge redistribution causes a certain number of electrons to transfer from the metal cluster to BNCNT, thereby enhancing electromagnetic wave absorption.

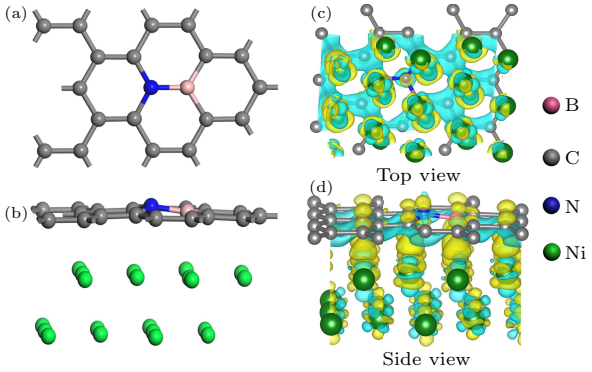

Fig. 6. Crystalline structure models of (a) BNCNT and (b) Ni@BNCNT. (c) and (d) Differential charge density diagrams for Ni@BNCNT (in units of 0.003e/Bohr^3).

Figure S8 shows the μ'–f and μ''–f plots of Ni@NCNT-800 and Ni@BNCNT-800. We observe that both exhibit closed μ' and μ'' values over 2–18 GHz, leading to their similar magnetic loss tangent values ($\tan\delta_m = \mu''/\mu'$). Thus, the enhanced electromagnetic wave property of Ni@BNCNT-800 is not relative to its magnetic loss. Notably, resonance peaks at about 12.0 GHz and 16.0 GHz are found in the μ''–f plots of both Ni@NCNT-800 and Ni@BNCNT-800. According to Aharoni's theory, the exchange resonance angular frequency can be expressed as[36,37]

$$\omega = \gamma\left(\frac{2A\mu_{kn}^2}{D^2 M_s} + H_c\right), \tag{4}$$

where A is the exchange constant, and μ_{kn} denotes the roots of the differential spherical Bessel functions; H_c denotes the coercivity in the magnetostatics field. Based on Aharoni's theory, the calculated exchange resonance frequencies are located at 12.3 and 16.7 GHz, consistent with the experimental measured frequencies. Thus, the exchange resonance contributes to the magnetic loss in Ni@NCNT-800 and Ni@BNCNT-800. Figure S9 shows the variations in C_0 [$C_0 = 2\pi\mu_0\sigma d^2/3 = \mu''(\mu')^{-2}f^{-1}$] for Ni@NCNT-800 and Ni@BNCNT-800 based on frequency. The values trend to become a constant at $f > 5$ GHz, and therefore the eddy effect partially contributes to the magnetic loss inNi@NCNT-800 and Ni@BNCNT-800. Based on the above discussion, the dielectric and magnetic losses are summarized in Fig. S10. Of these loss factors, enhanced conduction and polarization relaxation losses play dominant roles in the enhanced electromagnetic wave absorption characteristics of these materials.

The impedance matching characteristic is coordinately important to the electromagnetic wave absorption property of an absorber, in addition to dielectric and magnetic losses. The impedance coefficient M_z may be used to evaluate the impedance matching degree:[28]

$$M_z = \frac{2Z'_{in}}{|Z_{in}|^2 + 1}, \tag{5}$$

where Z'_{in} denotes the real part of the input impedance. We require M_z to be as close as possible to 1, as this means that all incident waves can penetrate to the first surface of the absorber with less microwave reflection, improving the impedance matching characteristics of the absorbing material. Figure S11 shows the M_z–f plots for Ni@NCNT-800 and Ni@BNCNT-800 over a range 2–18 GHz. We observe that the M_z of Ni@BNCNT-800 for each matching thickness (1.5–5.0 mm) is closer to 1 than that of Ni@NCNT-800. We can therefore conclude that the impedance matching characteristics of CNTs doped with B atoms are enhanced, leading to an enhancement in the absorber's electromagnetic wave absorption capability.[38–45]

In summary, we have successfully prepared B and N co-doped CNTs with embedded Ni nanoparticles, using nickel boride nanosheet/Ni metal nanoparticles as precursors, via a simple method. The experimental results show that the introduction of B atoms improves conduction, and polarization relaxation losses, as well as impedance matching characteristics. As a result, the B and N co-doped CNTs exhibit excellent electromagnetic wave absorption properties, with a minimal reflection loss of −37.5 dB at a matching thickness of 2.5 mm, and an efficient absorption bandwidth of 3.92 GHz at a matching thickness of 1.5 mm, superior to a sample with N-dopants alone. The *in*

situ B doping strategy presented in this work may pave the way for the design of high-performance electromagnetic wave absorbing materials.

References

[1] Yan L W, Hong C Q, Sun B Q, Zhao G D, Cheng Y H, Dong S, Zhang D Y and Zhang X H 2017 *ACS Appl. Mater. & Interfaces* **9** 6320
[2] Liu P B, Zhang Y Q, Yan J, Huang Y, Xia L and Guang Z X 2019 *Chem. Eng. J.* **368** 285
[3] Wang D T, Wang X C, Zhang X, Yuan H R and Chen Y J 2020 *Chin. Phys. Lett.* **37** 045201
[4] Jian X, Wu B, Wei Y F, Dou S X, Wang X L, He W D and Mahmood N 2016 *ACS Appl. Mater. & Interfaces* **8** 6101
[5] Yang M L, Yuan Y, Li Y, Sun X X, Wang S S, Liang L, Ning Y H, Li J J, Yin W L, Che R C and Li Y B 2020 *Carbon* **161** 517
[6] Andrey S, Andreev Mariya A, Kazakova A V, Ishchenko A G, Selyutin O B, Lapina V L and de Lacaillerie K J B D 2017 *Carbon* **114** 39
[7] Lin H Y, Zhu H, Guo H F and Yu L F 2007 *Mater. Lett.* **61** 3547
[8] Qing Y C, Zhou W C, Luo F and Zhu D M 2010 *Carbon* **48** 4074
[9] Li N, Huang G W, Li Y Q, Xiao H M, Feng Q P, Hu N and Fu S Y 2017 *ACS Appl. Mater. & Interfaces* **9** 2973
[10] Shen C and Zhao D 2001 *New Carbon Mater.* **16** 1
[11] Liu L L, Zhang S, Yan F, Li C Y, Zhu C L, Zhang X T and Chen Y J 2018 *ACS Appl. Mater. & Interfaces* **10** 14108
[12] Xu J, Shi Y N, Zhang X C, Yuan H R, Li B, Zhu C L, Zhang X T and Chen Y J 2020 *J. Mater. Chem. C* **8** 7847
[13] Zhang X C, Xu J, Yuan H R, Zhang S, Ouyang Q Y, Zhu C L, Zhang X T and Chen Y J 2019 *ACS Appl. Mater. & Interfaces* **11** 39100
[14] Li K Y, Sun H, Yuan H R, Zhang S, Zhang X, Zhu C L, Zhang X T and Chen Y J 2020 *J. Alloys Compd.* **821** 153267
[15] Ning M Q, Li J B, Kuang B Y, Wang C Z, Su D Z, Zhao Y J, Jin H B and Cao M S 2018 *Appl. Surf. Sci.* **447** 244
[16] Zhang X C, Zhang X, Yuan H R, Li K Y, Ouyang Q Y, Zhu C L, Zhang S and Chen Y J 2020 *Chem. Eng. J.* **383** 123208
[17] Ma X Z, Li K Y, Zhang X, Wei B, Yang H, Liu L N, Zhang M Y, Zhang X T and Chen Y J 2019 *J. Mater. Chem. A* **7** 14904
[18] Guo Y Y, Yuan P F, Zhang J N, Hu Y F, Amiinu I S, Wang X, Zhou J G, Xia H C, Song Z B, Xu Q and Mu S C 2018 *ACS Nano* **12** 1894
[19] Stephan O, Ajayan P M, Colliex C, Ph R, Lambert J M, Bernier P and Lefin P 1994 *Science* **266** 1683
[20] Feng J, Pu F Z, Li Z X, Li X H, Hu X Y and Bai J T 2016 *Carbon* **104** 214
[21] Quan B, Liang X H, Ji G B, Cheng Y, Liu W, Ma J N, Zhang Y N, Li D R and Xu G Y 2017 *J. Alloys Compd.* **728** 1065
[22] Panchakarla L S, Govindaraj A and Rao C N R 2010 *Inorg. Chim. Acta* **363** 4163
[23] Zhang X C, Yan F, Zhang S, Yuan H R, Zhu C L, Zhang X and Chen Y J 2018 *ACS Appl. Mater. & Interfaces* **10** 24920
[24] Nguyen T T H, Le V K, Minh C L and Nguyen N H 2017 *Comput. Theor. Chem.* **1100** 46
[25] Yan F, Zhang S, Zhang X, Li C Y, Zhu C L, Zhang X T and Chen Y J 2018 *J. Mater. Chem. C* **6** 12781
[26] Li Y J, Huang B L, Sun Y J, Luo M C, Yang Y, Qin Y N, Wang L, Li C J, Lv F, Zhang W Y and Guo S J 2019 *Small* **15** 1804212
[27] Chen B H, He X B, Yin F X, Wang H, Liu D J, Shi R X, Chen J N and Yin H W 2017 *Adv. Funct. Mater.* **27** 1700795
[28] Yang L J, Jiang S J, Zhao Y, Zhu L, Chen S, Wang X Z, Wu Q, Ma J, Ma Y W and Hu Z 2011 *Angew. Chem. Int. Ed.* **50** 7132
[29] Ozaki J, Kimura N, Anahara T and Oya A 2007 *Carbon* **45** 1847
[30] Feng J, Zong Y, Sun Y, Zhang Y, Yang X, Long G K, Wang Y, Li X H and Zheng X L 2018 *Chem. Eng. J.* **345** 441
[31] Wu Z C, Pei K, Xing L S, Yu X F, You W B and Che R C 2019 *Adv. Funct. Mater.* **29** 1901448
[32] Yuan H R, Li B, Zhu C L, Xie Y, Jiang Y J and Chen Y J 2020 *Appl. Phys. Lett.* **116** 153101
[33] Liu J W, Che R C, Chen H J, Zhang F, Xia F, Wu Q S and Wang M 2012 *Small* **8** 1214
[34] Liu Q H, Cao Q, Bi H, Liang C Y, Yuan K P, She W, Yang Y J and Che R C 2016 *Adv. Mater.* **28** 486
[35] Wen B, Cao M S, Lu M M, Cao W Q, Shi H L, Liu J, Wang X X, Jin H B, Fang X Y, Wang W Z and Yuan J 2014 *Adv. Mater.* **26** 3484
[36] Aharoni A 1991 *J. Appl. Phys.* **69** 7762
[37] Wilts C H, Lai S K C 1972 *IEEE Trans. Magn.* **8** 280
[38] Li X H, Feng J, Du Y P, Bai J T, Fan H M, Zhang H L, Peng Y and Li F S 2015 *J. Mater. Chem. A* **3** 5535
[39] Wang H, Dai Y Y, Gong W J, Geng D Y, Ma S, Li D, Liu W and Zhang Z D 2013 *Appl. Phys. Lett.* **102** 223113
[40] Wu Q L, Wang J, Jin H H, Yan T Y, Yi G Q, Su X G, Dai W and Wang X 2019 *Mater. Lett.* **244** 138
[41] Xiang J, Li J L, Zhang X H, Ye Q, Xu J H and Shen X Q 2014 *J. Mater. Chem. A* **2** 16905
[42] Zhang X F, Dong X L, Huang H, Liu Y Y, Wang W N, Zhu X G, Lv B and Lei J P 2006 *Appl. Phys. Lett.* **89** 053115
[43] Chen Y J, Xiao G, Wang T S, Ouyang Q Y, Qi L H, Ma Y, Gao P, Zhu C L, Cao M S and Jin H B 2011 *J. Phys. Chem. C* **115** 13603
[44] Sun G B, Wu H, Liao Q L and Zhang Y 2018 *Nano Res.* **11** 2689
[45] Wen F S, Hou H, Xiang J Y, Zhang X Y, Su Z B, Yuan S J and Liu Z Y 2015 *Carbon* **89** 372

Supplementary Information: Nitrogen and boron co-doped carbon nanotubes embedded with nickel nanoparticles as highly efficient electromagnetic wave absorbing materials

Xin Zhu[a](朱鑫), Feng Yan[a*](闫峰), Chunyan Li[a](李春燕), Lihong Qi[a](齐立红), Haoran Yuan[a](袁浩然), Yanfeng Liu[b](刘岩峰), Chunling Zhu[b*](朱春玲), Yujin Chen[a,b,c*](陈玉金)

[a] Key Laboratory of In-Fiber Integrated Optics, Ministry of Education and College of Science, Harbin Engineering University, Harbin 150001, China

[b] College of Materials Science and Chemical Engineering, Harbin Engineering University, Harbin 150001, China

[c] School of Materials Science and Engineering, Zhengzhou University, Zhengzhou 450001, China

*Corresponding authors: Email: chenyujin@hrbeu.edu.cn; yanfeng@hrbeu.edu.cn; zhuchunling@hrbeu.edu.cn.

EXPERIMETNAL SECTION

Synthesis of nickel boride. 0.0475 g of nickel chloride hexahydrate(NiCl2•6H2O) and 0.2 g of polyvinylpyrrolidone(Polyvinylpyrrolidone，Mw=55000）were put into a three-necked round-bottom flask, and then add 5ml of deionized water to the flask, stir for one hour, and continue to pass in Ar during the process. Then, 0.025 g $NaBH_4$ dissolved into 20 ml of deionized water was quickly added to the flask with a syringe, and the solution immediately turned black. Finally, the black precipitate was filtered and washed with deionized water several times, and freeze-dried to obtain nickel boride black powder.

Synthesis of Ni@BNCNT. The nickel boride powder and dicyandiamide were put into the porcelain boat at a ratio of 1:30, and heated to a certain temperature at a rate of 5 ℃/min under argon flow for 2 hour.

Synthesis of $Ni(OH)_2$. 1.83 g of nickel nitrate and 0.8 g of sodium hydroxide were added to a beaker containing 200 mL of deionized water. Then the light green precipitate was obtained. The precipitate was washed with water, and then centrifuged and dried at 40^{o}C.

Synthesis of Ni@NCNT. The preparation of Ni@NCNT was similar to that Ni@BNCNT except that the nickel boride was replaced with $Ni(OH)_2$. The annealing temperature was set to 800 ^oC.

Characterizations. The morphology and size of the synthesized samples were characterized by X-ray powder diffraction (XRD) using a X Pert Pro diffractometer with Cu Kα radiation (λ=1.5418 Å). The structures of the samples were analyzed by scanning electron microscope (SEM, SU70, Hitachi) and transmission electron microscopy (TEM, JEM-2100F, JEOL) with an emission voltage of 200 kV. Sample surface element analysis were taken on X-ray photoelectron spectrometer (KAlpha,Thermofisher Scienticfic Company) with Al Kα radiation generated at 12 kV and 150 W. Raman spectrometer was used to test the degree of graphitization of carbon nanotube on Lab RAM Aramis micro Raman spectrometer with an excitation wavelength at 488 nm. The chemical composition of the samples was determined by inductively coupled plasma-optical emission spectroscopy (ICP-OES, Optima 8000 PE). The magnetostatic properties of Ni@BNCNT and Ni@NCNT were measured at room temperature by a vibrating sample magnetometer (VSM, 7410 series, Lake Shore).

Calculations for the differential charge density. By using the Material studios (MS) software to establish the crystal structure model, find the initial structure model of the graphite layer in the MS software, doping with boron and nitrogen elements. The formula for differential charge density is:

$$\Delta\rho=\rho_{AB}-\rho_A-\rho_B \quad (S1)$$

In the formula, ρ_{AB} represents the charge density of several materials after bonding, ρ_A and ρ_B represent the individual charge density of A and B in the material, respectively. Based on density functional theory (DFT), this paper uses VASP (Vienna Ab-initio Simulation Package) software, one of the first-principles calculation codes, calculated the charge distribution of Ni and C atoms at the interface between Ni NPs and BNCNT. When calculating, set the plane wave cut-off energy E-cut to 400 eV and K-point to 1*1*1.

Electromagnetic parameter measurements. The electromagnetic wave absorption

parameters of the material, namely the relative complex permittivity and the relative complex permeability, are tested by using a vector network analyzer (model Anritsu MS4644A Vectorstar). Before testing, we need to calibrate the instrument: short circuit-open circuit-load-through, and then use the coaxial method to scan the sample in the frequency range of 2-18 GHz. The sample and the paraffin matrix are uniformly mixed according to a certain filler ratio, and the mixture is pressed into a cylindrical shape with an inner diameter of 3.0 mm, an outer diameter of 7.0 mm, and a thickness of 2 to 3 mm, then measure its electromagnetic parameters.

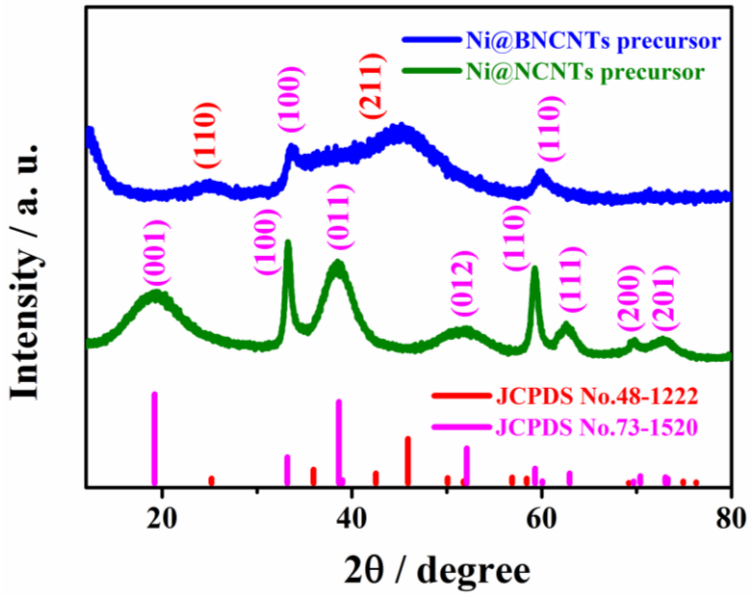

FIG. S1: XRD patterns of the precursors for Ni@BNCNTs and Ni@NCNTs.

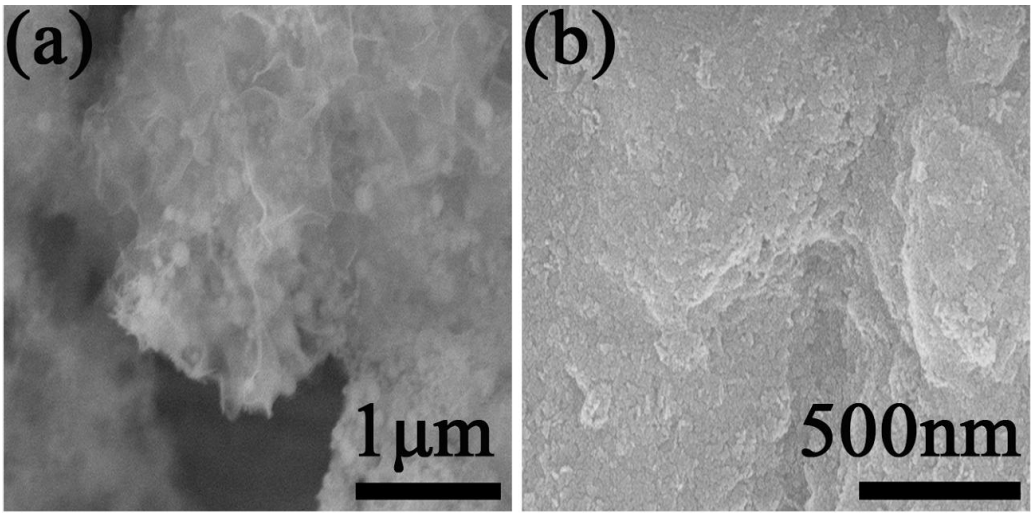

FIG. S2: SEM images of the precursor for (a) Ni@BNCNTs, and for (b) Ni@NCNTs.

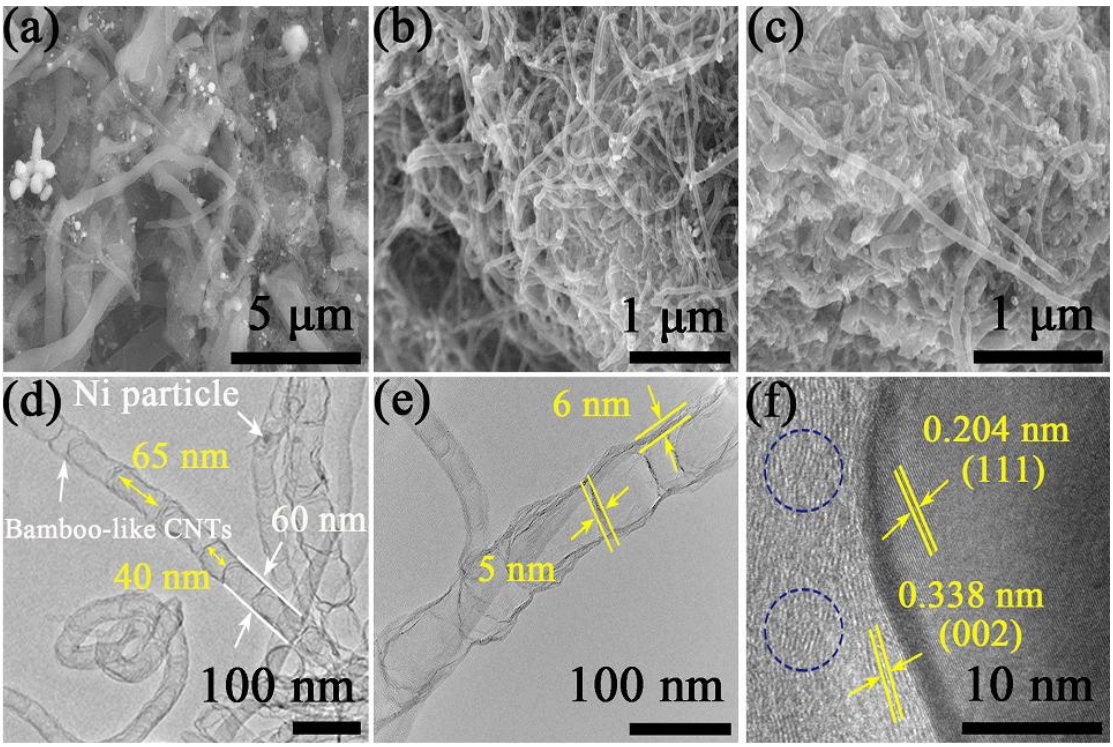

FIG. S3: SEM and TEM images of (a,d) Ni@NCNT-800, b,e) Ni@BNCNT-700, and (c,f) Ni@BNCNT-900.

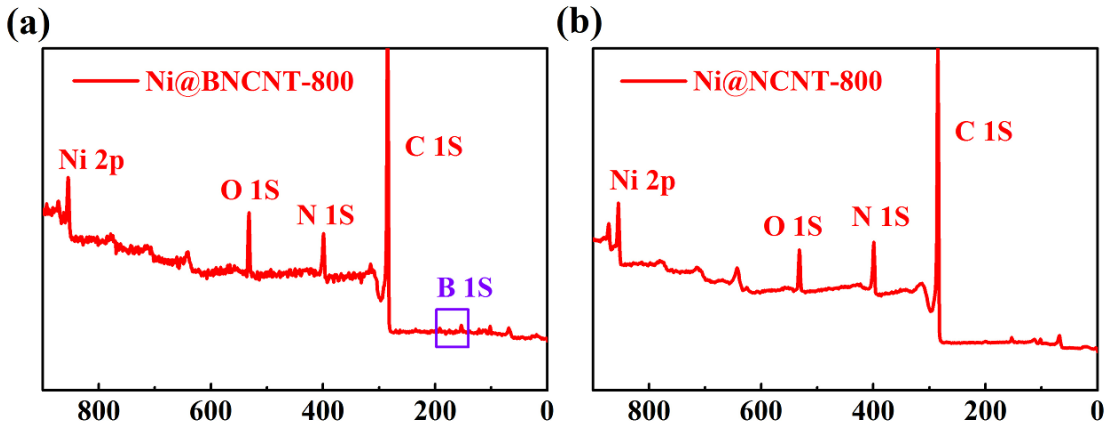

FIG. S4: The XPS survey spectrum of (a) Ni@BNCNT-800 and (b) Ni@NCNT-800.

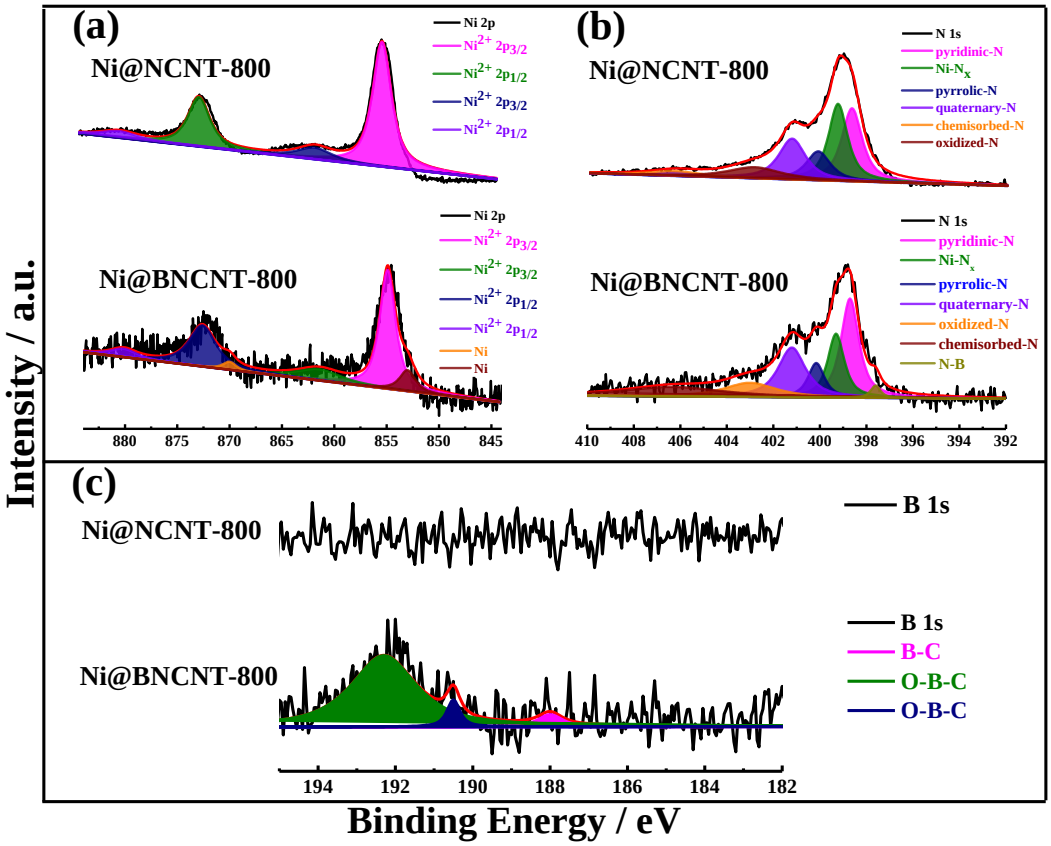

FIG. S5: (a) Ni 2p XPS spectra, (b) N 1s core-level XPS spectra, (c) B 1s core-level XPS spectra.

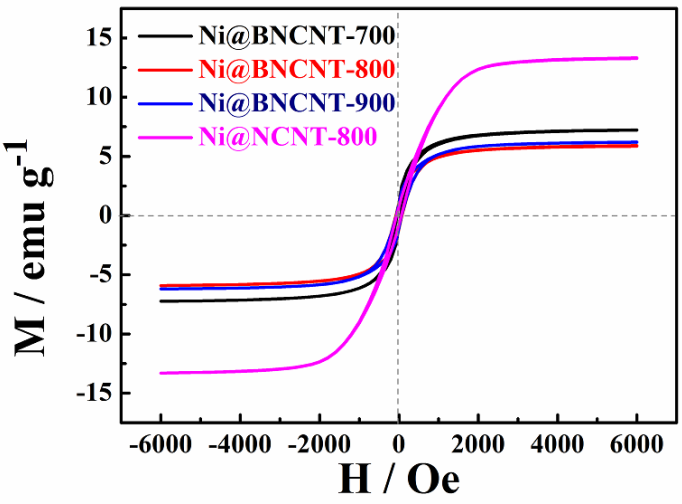

FIG. S6: Magnetization hysteresis loops of Ni@BNCNTs and Ni@NCNT-800.

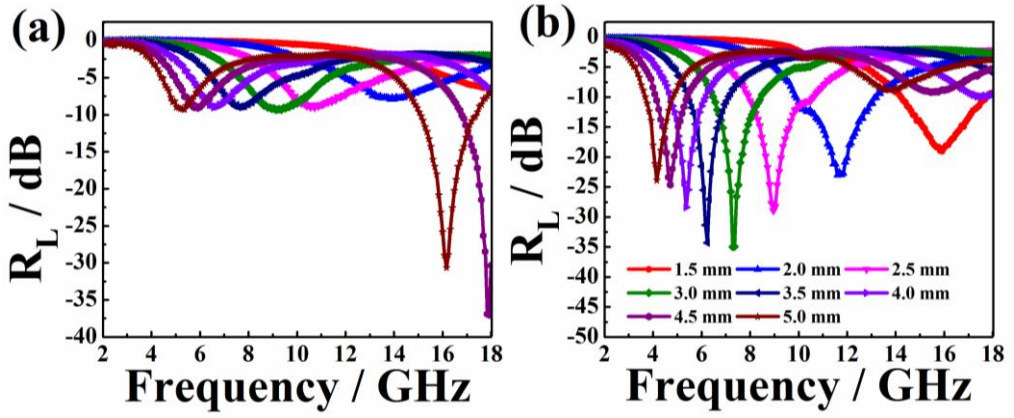

FIG. S7: Frequency-dependent R_L plots of (a) Ni@BNCNT-700 and (b) Ni@BNCNT-900 at d in range of 1.5 – 5.0 mm.

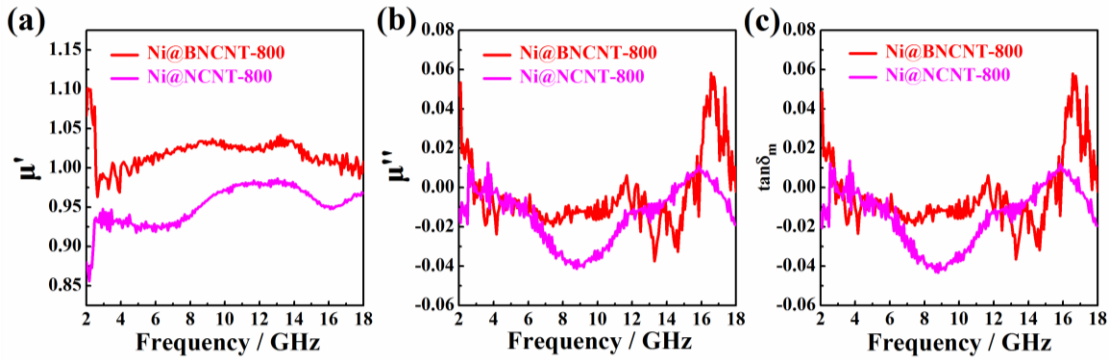

FIG. S8: (a) The real parts of the the complex permeabilities, (b) the imaginary parts of the complex permeabilities, and (c) the magnetic loss tangents of Ni@BNCNT-800 and Ni@NCNT-800.

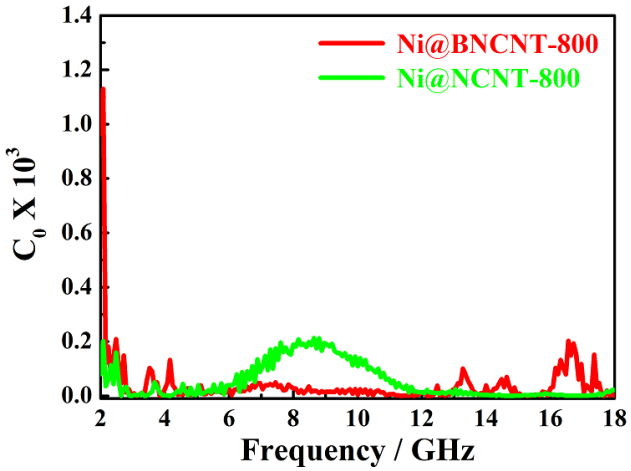

FIG. S9: $C_0 - f$ curves of Ni@BNCNT-800 and Ni@NCNT-800.

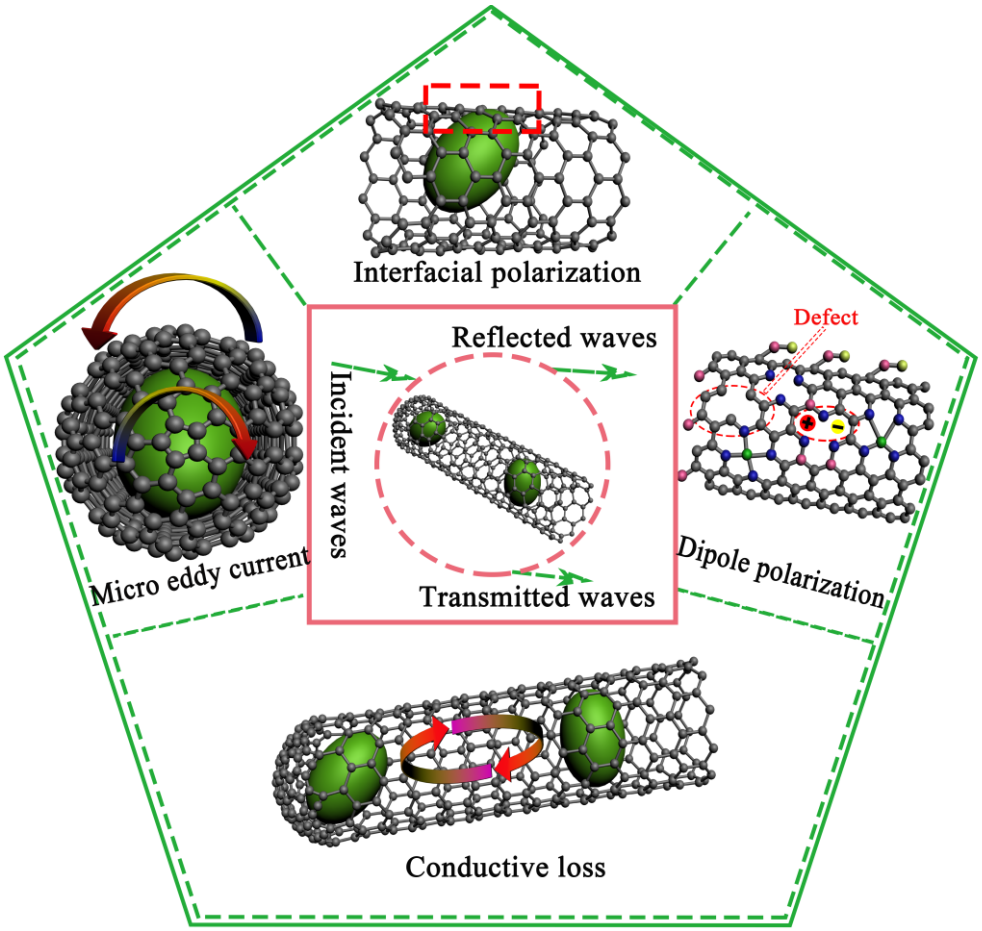

FIG. S10: Schematic illustration of the absorption mechanism for Ni@BNCNTs.

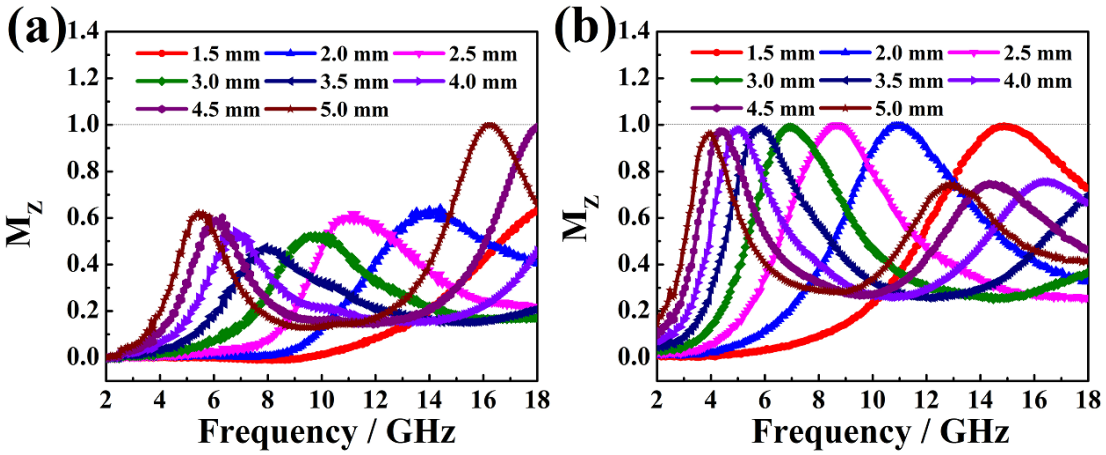

FIG. S11: M_Z-f plots of (a) Ni@NCNT-800 and (b) Ni@BNCNT-800.

Table S1 Comparison of EMW absorption properties of Ni@BNCNTs with those of the reported materials.

Samples	R_{Lmin} / dB	Thickness / mm	Filler rato / wt%	Ref.
Fe@CNTs	-22.7	3.5	20	7
MWCNT/CI	-16.9	1.5	50	8
Fe3O4/CNT (FCC14)	-43	1.5	30	9
CoNi/N-GCT	-41.1	3.5	25	14
Fe/NCNTs	-30.4	3.5	30	15
CoNi@NCNT	-49.8	3.5	20	16
Co/N-doped carbon nanofibers	-25.7	2.0	5	38
FeCo@C	-29	5	50	39
GO/CNT-Fe_3O_4	-37	5.0	30	40
Fe_3O_4/CNT	-25	5	88	41
CNTs/Ni	-22.89	5.0	30	10
Ni@C nanocapsules	-32	2.0	50	42
MoS_2 NS/U-NCNTs	-20.9	2.5	30	11
Fe_3O_4/carbon core/shell nanorods	-27.9	2.0	55	43
CoNi/GN	-30.1	2.0	60	44
Ni@BNCNTs	-37.5	2.5	25	This work

Table S2. The parameters of the samples according to H-N simulation.

Samples	α	β	t	σ_{fit}/S m^{-1}
Ni@BNCNT-700	0.67	0.96	0.14	0.05
Ni@BNCNT-800	0.31	0.9	0.49	0.24
Ni@BNCNT-900	0.54	1.0	0.30	0.12
Ni@NCNT-800	0.03	0.3	0.10	0.03